Spatial Atmospheric Pressure Atomic Layer Deposition of Tin Oxide as an Impermeable Electron Extraction Layer for Perovskite Solar Cells with Enhanced Thermal Stability

Lukas Hoffmann, Kai O. Brinkmann, Jessica Malerczyk, Detlef Rogalla, Tim Becker, Detlef Theirich, Ivan Shutsko, Patrick Görrn and Thomas Riedl

Final version published in:

ACS Applied Materials & Interfaces **2018,** 10(6), 6006-6013
https://doi.org/10.1021/acsami.7b17701

Spatial Atmospheric Pressure Atomic Layer Deposition of Tin Oxide as Impermeable Electron Extraction Layer for Perovskite Solar Cells with Enhanced Thermal Stability

Lukas Hoffmann[1], Kai O. Brinkmann[1]*, Jessica Malerczyk[1], Detlef Rogalla[2], Tim Becker[1], Detlef Theirich[1], Ivan Shutsko[3], Patrick Görrn[3], Thomas Riedl[1]**

[1] Chair of Electronic Devices, University of Wuppertal, Rainer-Gruenter-Strasse 21, 42119 Wuppertal, Germany

[2] RUBION, University of Bochum, Universitätsstr. 150, 44801 Bochum, Germany

[3] Chair of Large Area Optoelectronics, University of Wuppertal, Rainer-Gruenter-Strasse 21, 42119 Wuppertal, Germany

Spatial ALD, tin oxide, roll-to-roll compatible solar cells, perovskite solar cells, stability of perovskite solar cells

ABSTRACT.

Despite the notable success of hybrid halide perovskite-based solar cells (PSCs), their long-term stability is still a key-issue. Aside from optimizing the photo-active perovskite, the cell design states a powerful lever to improve stability under various stress conditions. Dedicated electrically conductive diffusion barriers inside the cell stack, that counteract the ingress of moisture and prevent the migration of corrosive halogen species, can substantially improve ambient and thermal stability. While atomic layer deposition (ALD) is excellently suited to prepare such functional layers, ALD suffers from the requirement of vacuum and only allows for a very limited throughput. Here, we demonstrate for the first time spatial ALD grown SnO_x at atmospheric pressure as impermeable electron extraction layers for perovskite solar cells. We achieve similar optical transmittance and electrical conductivity as in SnO_x grown by conventional vacuum based ALD. A low deposition temperature of 80°C and a high substrate speed of 2.4 m/min yield SnO_x layers with a low water vapor transmission rate of ~ 10^{-4} $gm^{-2}d^{-1}$ (at 60°C / 60% r.H.). Thereby, in perovskite solar cells, dense hybrid Al:ZnO/SnO_x electron extraction layers are created that are the key for stable cell characteristics beyond 1000 h in ambient air and over 3000 h at 60°C. Most notably, our work of introducing spatial ALD at atmospheric pressure paves the way to the future roll-to-roll manufacturing of stable perovskite solar cells.

1. INTRODUCTION

Within the past few years hybrid halide perovskite solar cells (PSCs) have seen an unprecedented progress as power conversion efficiencies (PCEs) have reached a level beyond 20% [1–4]. Nevertheless, a serious concern about stability is coming along with PSCs, as the photo-active

perovskites tend to decompose upon exposure to moisture and/or elevated temperatures [5–10]. On top of that, halide containing species resulting from the decomposition of the perovskite can corrode metal electrodes and thereby drastically compromise the device stability [11,12]. Recently, a number of approaches have been proposed to mitigate these stability issues. Aside from the use of alternative electrodes like carbon [13], a very promising concept is based on the introduction of a protection layer as an electronically functional part of the solar cell stack. The purpose of these layers is to shield the rest of the device from ambient gases and simultaneously to prevent corrosive perovskite constituents to degrade the electrode. Organic, metal-oxide and even modified two-dimensional perovskite capping layers have been considered for this aim [14–21].

Although, all of those strategies yield some kind of stability improvement, the respective PSCs still face notable degradation on the long run, especially when exposed to elevated temperatures. This is most likely related to the limited barrier properties of the proposed protecting layers. In general, metal-oxide layers prepared by atomic layer deposition (ALD) state the most promising avenue to realize functional protection layers, as ALD is known to afford extremely dense, conformal and pinhole free layers [22–24].

The plethora of studies on permeation barriers prepared by ALD is focused on insulating materials, like Al_2O_3 etc.. A few authors have attempted to introduce ALD-grown Al_2O_3 into a PSC to protect and to stabilize the photo-active perovskite [25–27]. While some improvement has been demonstrated, the use of insulating layers inside a device stack is limited to at best a few monolayers, through which carriers can still tunnel. For thicker layers (> 1 nm) a severe deterioration of the device characteristics is typically observed. It is clear that these ultra-thin protection layers do not form serious permeation barriers [26]. Likewise Kim et al. introduced ALD

grown titanium oxide interlayers for stabilization, albeit at the cost of compromised solar cell performance due to the poor electrical conductivity of the low temperature TiO_x [28]. Specifically, the resulting solar cells show a notable series resistance and a relatively low FF <50%.

Recently, we have demonstrated transparent and electrically conductive permeation barriers based on tin oxide grown by ALD [29]. We could show that these SnO_x layers can be introduced in the stack of a PSC without compromising cell performance where they efficiently prevented the ingress of moisture and at the same time suppressed the decomposition of the perovskite active layer [30]. Concomitantly, the SnO_x layer has been shown to protect sensitive metal electrodes against the corrosive halide constituents of the perovskite [31]. Thereby, we were able to present highly robust opaque and semitransparent PSCs [30,32]. As an important note, the efficiency of PSCs that were only encapsulated with an external permeation barrier, i.e. outside the cell stack, degraded swiftly under the same stress conditions.

The most severe drawback of our SnO_x layers is their preparation by classical batch based ALD (B-ALD) under vacuum conditions. The limitations of classical ALD contradict the paradigm of low-cost, high-throughput preparation at atmospheric pressure, which is a particular selling point frequently associated with PSCs. There are efforts to overcome the limits of classical B-ALD by the introduction of spatial ALD (S-ALD), which can operate in a continuous fashion at atmospheric pressure [33]. Very recently, we have demonstrated that high-performance gas diffusion barriers based on Al_2O_3 can be prepared by S-ALD at atmospheric pressure [34].

In this work, we introduce for the first time S-ALD grown SnO_x at atmospheric pressure as impermeable electron extraction layers in perovskite solar cells. Thereby, we render the use of these key stabilizing constituents to become compatible with the demands of even roll-to-roll manufacturing. We evidence, that up to a web speed of 2.4 m/min, we can achieve the benefits of

continuous processing without sacrificing the excellent electrical and barrier properties of SnO_x known from vacuum based B-ALD. Moreover, we demonstrate that the S-ALD SnO_x layer can be grown in a continuous fashion at temperatures as low as 80°C on top of the photo-active perovskite material. The resulting PSCs show an outstanding long-term stability in excess of 3000 hours at elevated temperature.

2. EXPERIMENTAL

Tin oxide thin films were deposited in a home-built S-ALD system, already described in former work [34]. Tetrakis(dimethylamino)tin(IV) (TDMASn) (99.99%, Strem Chemicals) and water were used as precursors. A schematic of the S-ALD setup is shown in Figure 1a. Both precursors were kept in a bubbler at room temperature. N_2 was used as purge gas. Typically, a flow of 150 sccm of N_2 through the TDMASn-bubbler and 8 sccm of N_2 through the H_2O-bubbler have been used with a total gas flow at each precursor line of 2000 sccm. Note, the corresponding density of water molecules is about 3×10^{15} cm^{-3} in the delivery zone of the water precursor in the S-ALD setup. This concentration is more than an order of magnitude below the levels of 1×10^{17} cm^{-3}, that have earlier been identified for the onset of decomposition of an unprotected MAPbI3 layer [35,36]. The deposition temperature has been varied between 80 and 150°C, and the substrate velocity has been varied between 5 mm/s and 160 mm/s. For reference, SnO_x layers were deposited in a commercial ALD system (Beneq ALD TFS 200) at a base pressure of 1.5 mbar. Further details of the classical ALD growth process for SnO_x can be found in Ref. [29].

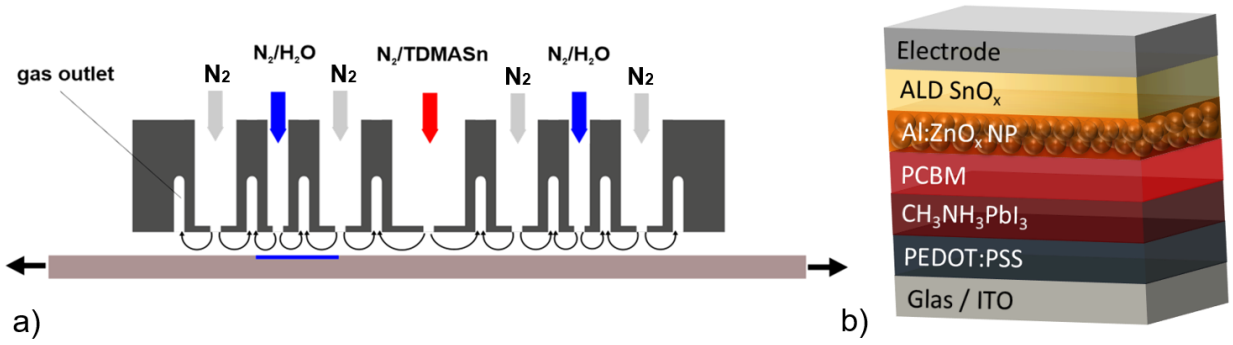

Figure 1. a) Schematic of the spatial ALD assembly. b) p-i-n solar cell stack used in this work.

The inverted perovskite solar cells (p-i-n PSCs) are based on a glass/ITO/ PEDOT:PSS/$CH_3NH_3PbI_3$/PCBM/AZO/SnO_x/Ag sequence (see Figure 1b). First, PEDOT:PSS (AI4083) has been spin coated in ambient air and has been dried on a hot plate at 120°C for 20 min in an N_2-environment. The $CH_3NH_3PbI_3$ perovskite layers have been spin coated under inert atmosphere from a commercially available precursor solution (Ossila Ltd.) and have been post-annealed at 100°C for 80 min. Afterwards, PCBM (American Dye Source Inc., ADS61BFA) was spin coated from a solution in chlorobenzene (1000 rpm, 30s, concentration: 100 mg/ml). The AZO layer has been spin-coated from a commercial nanoparticle dispersion (8000 rpm, 60s, 2.5 wt% in isopropanol, Prod. No. 8045, Avantama AG, Switzerland). The size of the AZO nanoparticles is in the range of 12-18nm. SnO_x layers were deposited by S-ALD or B-ALD as described above. Finally, Ag electrodes (thickness: 100 nm) were thermally evaporated. J/V characterizations and stabilized power output of the respective solar cells were conducted without encapsulation in air with a Keithley 2400-C source meter and a solar simulator (300W Newport, model 91160, AM1.5G). Calibration to 100 $mWcm^{-2}$ was done with a commercial IEC 60904-9 compliant and certified Si reference cell (Rera Systems).

Rutherford backscattering (RBS) and nuclear reaction analysis (NRA) were performed at the 4 MV tandem accelerator of the RUBION facility (University of Bochum, Germany). For RBS a

2 MeV $^4He^+$ ion beam (beam current of 20−40 nA) in combination with a silicon surface barrier detector at an angle of 160° was used. For a higher sensitivity to atoms with low atomic number, i.e. C, N and O, the complementary NRA measurements were performed with a 1 MeV $^2H^+$ beam (beam current of 40−80 nA). A silicon surface barrier detector was placed at an angle of 135° and was shielded by a 6 micrometer Ni foil to eliminate scattered particles.

The water vapor transmission rate (WVTR) was measured using an optical calcium test on 7×7cm^2 glass substrates. Details of the Ca-test can be found in our previous work [34,37]. The electrical conductivity of our SnO_x layers was measured with the Van der Pauw method.

The transmission/reflection spectra of the SnO_x films deposited by ALD were measured with a deuterium halogen lamp (DH-2000-BAL, Ocean Optics, 1 mW cm^{-2}) and a fiber spectrometer (USB 2000+XR1-ES, Ocean Optics, from 186 to 1041 nm). Each spectrum is an average of 300 measurements at 5 different positions on the sample. The absorption spectra ($A(\lambda)$) were calculated directly from transmittance ($T(\lambda)$) and reflectance ($R(\lambda)$) spectra using the following equation: $A(\lambda) = 1\text{-}T(\lambda)\text{-}R(\lambda)$.

EQE measurements were carried out with a home-built set-up using probe light from a tunable monochromatic light-source consisting of a 50 W tungsten halogen lamp and a monochromator (MSH-150, LOT-Quantum Design GmbH). The current response of the PSC devices was measured using a lock-in amplifier (5610B, NF Electronic Instruments).

3. RESULTS AND DISCUSSION

3.1 PROPERTIES OF TIN OXIDE GROWN BY S-ALD

Tin oxide thin films were deposited in an S-ALD system at atmospheric pressure. The S-ALD system is described in more detail in previous reports [34]. The layout of the S-ALD coating head is

shown in Figure 1. Briefly, in S-ALD the moving substrate is sequentially exposed to the precursors emerging from the spatially separated precursor outlets in the S-ALD head. Thereby, the time-sequenced delivery of the precursors to a static substrate, as in conventional B-ALD is mimicked. As a starting point, the substrate speed was set to 20 mm/s (= 1.2 m/min) and the process temperature was 80°C. The ALD-typical self-limiting growth behavior at these processing conditions has been verified (Figure S1, supporting information). The selected N_2–gas flows of 50 sccm (through the TDMASn-bubbler) and 5 sccm (through the H_2O Bubbler) are clearly within the respective saturation regime with a growth per cycle (GPC) of (0.15 ± 0.01) nm.

Table 1 Comparison of the film properties of tin oxide layers deposited via spatial atmospheric pressure ALD (S-ALD) and low pressure batch ALD (B-ALD). In both cases, TDMASn and H_2O were used as precursors at a deposition temperature of 80°C. The substrate speed in the S-ALD process was 20 mm/s.

	S-ALD	B-ALD
GPC / nm	0.15	0.11
Refractive index n (at 632 nm)	1.88	1.89
Optical Bandgap / eV	3.8	3.8
Electrical conductivity / Scm^{-1}	10^{-4}	10^{-4}
WVTR / $gm^{-2}d^{-1}$ (at 60°C / 60% r.H.)	2×10^{-4}	4×10^{-4}

The properties of SnO_x layers grown by S-ALD and B-ALD are compared in Table 1. Obviously, S-ALD yields a somewhat higher GPC compared to B-ALD. Note, higher growth rates of atmospheric pressure ALD at low temperature vs. classical vacuum based ALD have been found

before for other metal oxides, e.g. Al_2O_3 or ZnO [37,38], and have been attributed to an excess of adsorbed water which leads to some additional CVD type of growth. In our earlier work we have studied the GPC in the S-ALD of SnO_x (from TDMASn/H_2O) at varied deposition temperature [39]. Specifically, the GPC varied from 0.15 nm (at 80°C) to 0.07 nm (at 150°C).

The optical properties of the SnO_x layers have been assessed by absorption spectroscopy and spectral ellipsometry. The respective absorption spectra for SnO_x grown by B-ALD and S-ALD at various deposition temperatures are shown in the supporting information (Figure S2). The optical band-gap is determined from the respective Tauc-plots. A band gap of 3.8 eV was derived for SnO_x deposited by both S-ALD and B-ALD at 80°C. With increasing the deposition temperature the optical band-gap decreases (to 3.2 eV at 150°C deposition temperature) and a notable sub-band-gap absorption is found. A similar behavior has been previously reported [40] in B-ALD grown SnO_x layers and has been attributed to an increased density of sub-gap defects related to oxygen deficiency. In any case, a 20 nm thick SnO_x layer based on S-ALD show similar neglectable absorption in the spectral range of 430-780 nm as its low pressure counterpart.

The refractive indices of the S-ALD (1.88 @ 633 nm) and B-ALD (1.89) layers are quite similar. Moreover, within the accuracy of the experiment the S-ALD process yields SnO_x that show the same permeation barrier properties (water vapor transmission rate: WVTR = 2×10^{-4} $gm^{-2}d^{-1}$) and electrical conductivity ($\sigma = 10^{-4}$ S/cm) as their analogues grown by vacuum based B-ALD. For thin SnO_x layers of 20 nm, their electrical conductivity allows to estimate a very low specific series resistance of 0.02 Ωcm^2, which is not expected to infer any notable loss of voltage in a PSC.

3.2. S-ALD TIN OXIDE IN PEROVSKITE SOLAR CELLS.

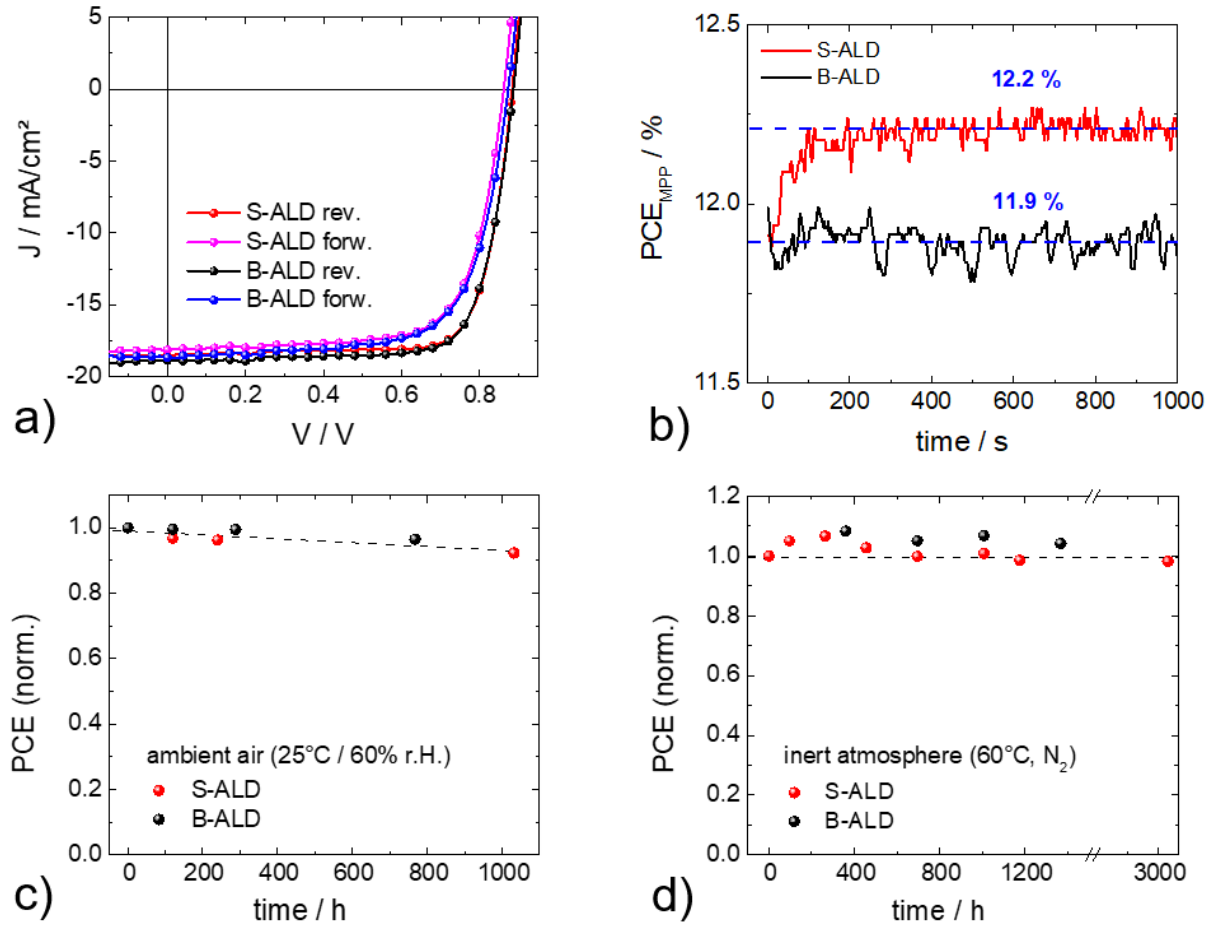

Figure 2. Comparison of PSCs incorporating SnO_x grown by B-ALD and S-ALD at 80°C. For the S-ALD a substrate velocity of 20 mm/s has been used. *J/V* characteristics (a) and stabilized power output (b). All related current density data were derived from EQE measurements (see Figure S3). PCE vs. time of storage in ambient air (25°C, 60% r.H.) (c) and at elevated temperature (60°C, inert atmosphere) (d).

Table 2. Solar cell characteristics corresponding to the representative *J/V* curves shown in Figure 2a for PSCs based on SnO_x grown by B-ALD and S-ALD. Current density data has been derived from EQE measurements. Statistical data for a set of samples can be found in the supporting information (Figure S4, Table S1).

	reverse				forward			
	PCE / %	**FF / %**	**V_{OC} / V**	**J_{SC} / mA/cm²**	**PCE / %**	**FF / %**	**V_{OC} / V**	**J_{SC} / mA/cm²**
S-ALD	12.7	77.7	0.88	18.6	11.2	71.6	0.86	18.2
B-ALD	12.6	75.6	0.89	18.8	11.2	69.9	0.87	18.5

The characteristics of representative PSCs incorporating an impermeable SnO_x electron extraction layer prepared by S-ALD and B-ALD are shown in Figure 2a,b. The typical solar cell figures as derived from the *J/V*-data are compared in Table 2. Note, all current density data were calibrated with dedicated EQE measurements. The corresponding EQE spectra are shown in the supplementary information (Figure S3). Both sets of samples show a remarkable similarity in their cell characteristics. This is even the more notable, as the S-ALD technique now paves the way to harvest the benefits of impermeable functional ALD layers even for high-throughput manufacturing.

In order to compare the stability of the PSCs, mono-stress tests under ambient conditions (25°C / 60% r.H.) (Figure 2c) and at elevated temperature (60°C, inert atmosphere) (Figure 2d) were conducted. Strikingly, under both conditions, excellent long-term stability of PSCs based on SnO_x grown by S-ALD is afforded. Note, for PSCs without the SnO_x layer, the devices degrade within tens of hours under ambient conditions (25°C / 60% r.H.) and within 200h at elevated

temperature (60°C, inert atmosphere) [30]. Please see Figure S5 for a full set of cell characteristics (J_{sc}, V_{oc}, *FF*) during temperature mono stress testing.

Taken together, SnO_x prepared by S-ALD affords PSCs with outstanding thermal stability even on a time scale of > 3000 h without noticeable decay in cell characteristics. In an aim to exploit the continuous S-ALD process for a roll-to-roll processing in the future, limitations regarding processing speed in S-ALD are of interest.

3.3 DEPOSITION SPEED IN S-ALD

We now evaluate the role of substrate speed in S-ALD on the functionality and stability of the resulting PSCs. First, the GPC vs. substrate speed is studied at otherwise fixed process parameters, e.g. gas flows (Figure 3a). Obviously, the GPC is constant for a substrate speed below 60 mm/s. Further increasing the speed results in a reduction of the GPC, as the precursor dose is no longer sufficient to fully saturate the reactive surface sites. The decay of GPC with increasing the substrate speed was approximated with $GPC = GPC_{sat} \times (1 - \exp(a\, t^q))$, similar to an equation proposed by Poodt et al. [41]. Here, GPC_{sat} represents the GPC at low substrate speeds, *t* is the precursor exposure time and *a* and *q* are fit parameters. For a further discussion see Refs. [34,41].

In addition to the drop in GPC, the refractive index decreases with increasing the substrate speed, i.e. from 1.88 at 20mm/s to 1.80 at 160 mm/s, indicating not fully-saturated ALD film growth and a lower film density. In principle, the regime of constant GPC can be extended to even higher substrate speeds by further increasing the amount of precursor delivered to the precursor exposure zone (e.g. by increasing the flow of carrier gas through the bubbler). At the same time, higher amounts of precursor would require higher purge gas flows or a spatial extension of the respective

purge gas zones. Unfortunately, both these possibilities cannot be tested due to limitations of our home-built S-ALD system.

Aside from the changes of layer properties towards higher processing speeds a further important characteristic of the ALD growth process is affected. It has to be noted that in the PSCs the SnO_x layer is deposited on top of a porous Al:ZnO layer, that has been cast on top of the PCBM from a dispersion of nanoparticles. ALD in general is known for its conformal coating properties of high-aspect ratio structures and even porous materials. With increasing the substrate speed the exposure time of the porous layer to the respective precursor species in the S-ALD process is reduced. Thereby the time for diffusion of precursors into the pores of the AZO layer is shortened. As suggested earlier [30], the functionality of the AZO/SnO_x hybrid layer as a permeation barrier relies critically on the penetration of ALD precursors into the pores of the AZO layer and the concomitant growth of SnO_x inside these pores. To further study the consequences of increased substrate speed, we analysed the resulting AZO/SnO_x hybrid layers by Rutherford Backscattering (RBS). The degree of penetration of tin atoms into the pores of the AZO layer becomes obvious form the Sn related RBS spectra (Figure 3b). For relatively small substrate speeds of 20 mm/s and 40 mm/s the Sn-peak in the RBS spectrum shows a notable shoulder, indicating the penetration of tin atoms into the AZO layer underneath. As these Sn-atoms are located further away from the surface (i.e. deeper inside the AZO layer) they cause backscattered ions with less energy (i.e. smaller channel number). On the contrary, for SnO_x grown at elevated substrate speed of 80 mm/s, a symmetric Sn-peak is found, indicating a substantially reduced penetration of tin into the pores of the AZO layer. Note, for SnO_x grown on a flat, non-porous substrates the tin RBS spectrum is fully symmetric, regardless of substrate speed. A schematic of the penetration of SnO_x inside the AZO is shown in Figure 3c.

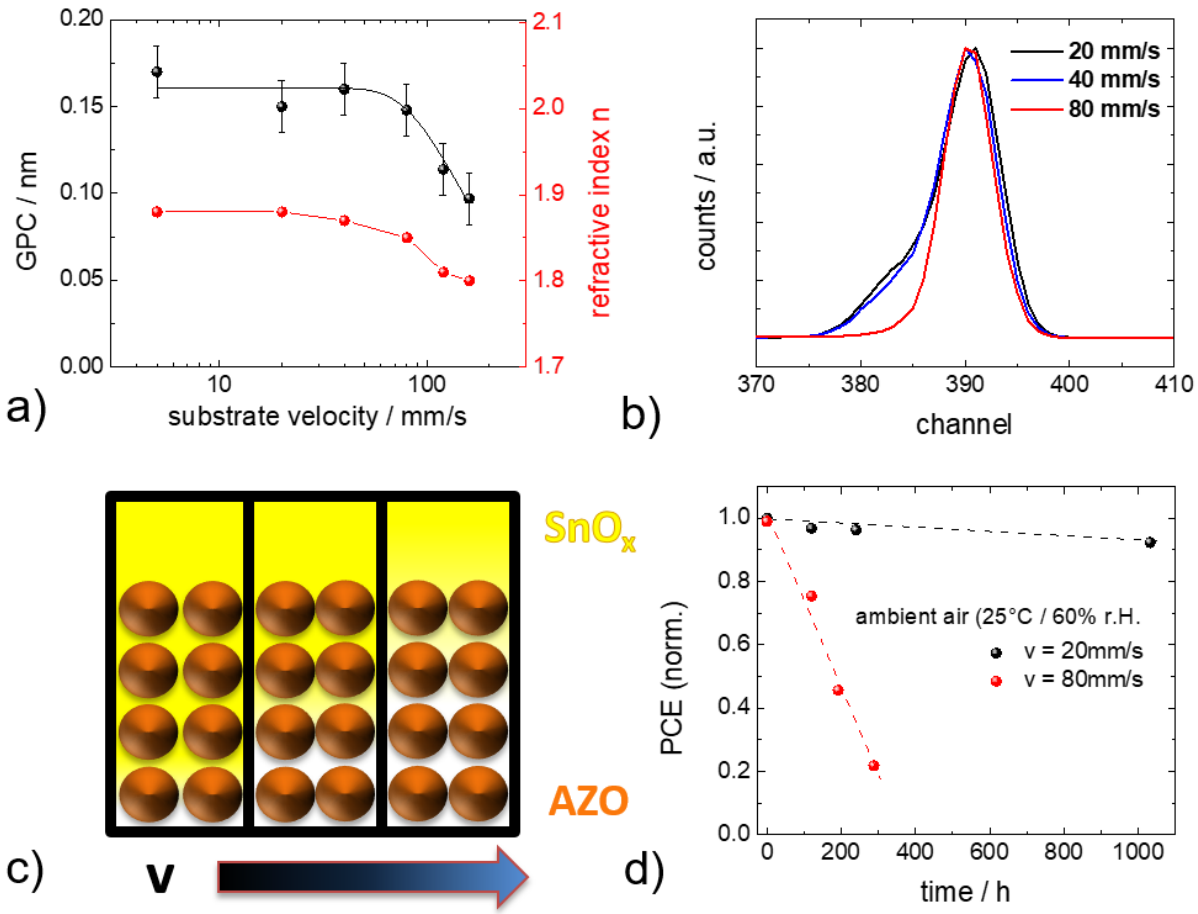

Figure 3. GPC and refractive index vs. substrate velocity at 80°C deposition temperature (a). RBS signal related to tin of the hybrid AZO/SnO_x layer for SnO_x deposited at varied substrate speed (b). Note, the Sn-spectra were normalized. Schematic of the diffusion of SnO_x (yellow) inside the AZO NP-layer (c). Normalized PCE vs. time of storage in ambient air (25°C, 60% r.H.) for solar cells with SnO_x layer grown at 20 mm/s and 80 mm/s, respectively (d).

As a consequence of the penetration of the SnO_x into the AZO pores, the barrier properties of the resulting AZO/SnO_x hybrid layers are substantially better than those where the SnO_x has been prepared at elevated substrate speed without notable pore filling. In addition, the WVTR of SnO_x single layers grown at 80 mm/s show inferior permeation barrier properties

(WVTR ~ 4×10^{-3} $gm^{-2}d^{-1}$) compared to their analogue grown at lower speed. This indicates an overall deterioration of layer density at elevated substrate speed, in agreement with the observed drop of the refractive index as discussed above.

As a result, the lifetime of PSCs based on the respective AZO/SnO_x is critically affected by the choice of substrate speed, when the devices are exposed to ambient air (25°C / 60 % r.H) (Figure 3d). The PCE of the PSCs based on the SnO_x grown at a substrate speed of 80mm/s, which does not afford filling of the AZO pores, decreases dramatically within the first 300 hours in air, while those cells, in which the SnO_x has been grown at 20 mm/s show only minimum degradation even after more than 1000 hours.

3.4 EFFECT OF DEPOSITION TEMPERATURE

While we have found that increasing the substrate speed compromises the barrier properties of the AZO/SnO_x hybrid layer, deposition temperature is a likewise critical parameter. For other material systems, an elevated growth temperature has been shown to have a beneficial impact on the layer density, electrical conductivity and reduced concentration of precursor residues of the resulting ALD layers [29,34,42]. The effect of substrate temperature on the electrical conductivity of SnO_x grown by both B-ALD and S-ALD using H_2O as oxidant has been studied previously [29,39]. For S-ALD SnO_x, the electrical conductivity remained in the range of 10^{-4}-10^{-3} S/cm for a growth temperature between 80-165°C. To analyze the influence of deposition temperature in case of our SnO_x layers grown by S-ALD, we performed a series of RBS studies. Thereby, we identify an elevated level of carbon (~20%) and nitrogen (~5%) residues in layers grown at 80°C (Table S2). For increasing the processing temperature to 120°C and 150°C, the content of Carbon / Nitrogen is significantly reduced to levels of 0.3% / 0.1% and 0.1% / <0.1%, respectively. At the same time,

the areal density of tin atoms (for a 20 nm thick layer) increases from 3.5×10^{16} atoms / cm² to 3.8×10^{16} atoms / cm² with increasing the deposition temperature. Concomitantly, the WVTR decreases by about an order of magnitude from ~10^{-4} $gm^{-2}d^{-1}$ to about 10^{-5} $gm^{-2}d^{-1}$ (Figure 4a).

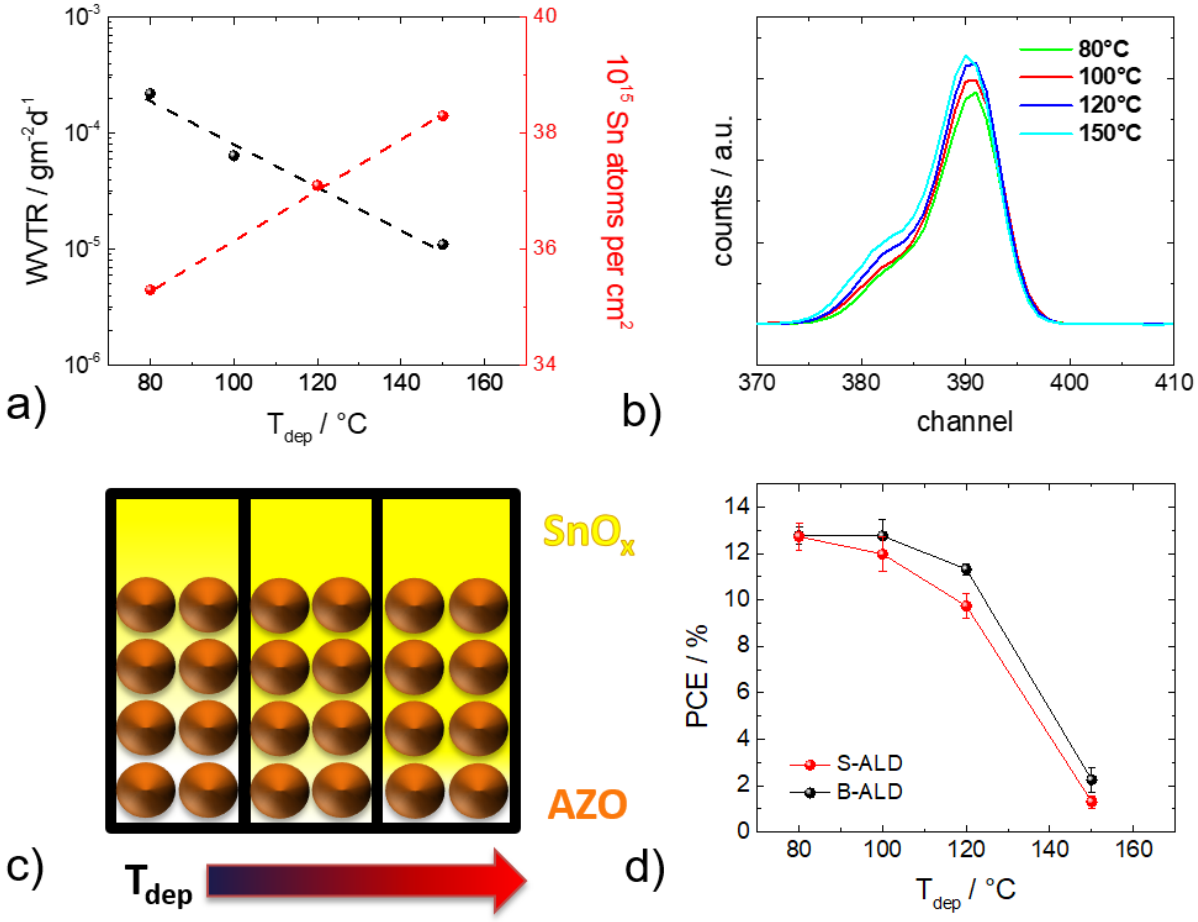

Figure 4. Impact of deposition temperature on SnO_x as well as on the solar cell. Water vapor transmission rate of SnO_x thin films (layer thickness: 100 nm)) and tin atom density (by Rutherford Backscattering) for neat S-ALD SnO_x layers of each 20 nm thickness (a). RBS spectra of Sn measured on AZO (60 nm) / SnO_x hybrid layers with increasing deposition temperature (b). The corresponding partial growth of SnO_x inside the pores of the AZO layer is schematically shown in

(c). PCE of the corresponding PSCs based on SnO_x grown at various temperatures (d). The substrate speed was 20 mm/s in this set of experiments.

Moreover, for the SnO_x/AZO bi-layers the characteristic shoulder in the RBS spectra towards lower channel numbers indicating the partial growth of SnO_x in the pores of the AZO layer shows a notable dependence on the deposition temperature (Figure 4b). Obviously, higher deposition temperatures infer an increased penetration of the SnO_x into the porous AZO (Figure 4c). This is very likely due to the thermally activated precursor diffusion [19].

Owing to the improved mass density, lowered WVTR and better pore filling of the SnO_x, increasing the deposition temperature appears to be attractive for the application in PSCs. Unfortunately, temperatures in excess of 100°C result in PSCs with substantially deteriorated characteristics (Figure 4d and Figure S6). Here, it is important to note that the post-deposition annealing of the perovskite layers was done at 100°C. It has been shown very recently, that for $MAPbI_3$ at temperatures higher than 100°C, thermal degradation is happening at the perovskite surface within minutes time [20,21]. For both S-ALD and B-ALD some exposure-time to the growth temperature prior to the actual deposition is technologically inevitable. Thus, the observed deterioration of our PSC at an ALD deposition temperature >100°C is very likely related to the thermal instability of the perovskite. To further exploit the superior properties of SnO_x grown at T > 100°C, the use of more temperature stable perovskite materials could be very rewarding, but are beyond the scope of this work.

Taken together, an optimum temperature window between 80-100°C affords the best PSC characteristics. At the same time, the barrier properties of the AZO/SnO_x hybrid layers grown by S-ALD in this temperature range provide an outstanding long-term cell stability. .

4. CONCLUSION

In summary, we have demonstrated that spatial ALD at atmospheric pressure affords SnO_x with similar optical and electrical properties as their analogues deposited by conventional vacuum based ALD. We unraveled the specific influence of deposition speed and temperature on the ability to form particularly dense hybrid AZO/SnO_x electron extraction layers in perovskite solar cells. We identified a low deposition temperature of 80°C as optimum choice. The substrate speed can be as high as 2.4 m/min, without sacrificing material properties. The low water vapor transmission rate of the SnO_x layers (~ 10^{-4} $gm^{-2}d^{-1}$) renders them excellent permeation barriers that limit the ingress of moisture into the devices. Most significantly, the SnO_x simultaneously forms a shield that protects constituents of the cell against corrosive halide containing perovskite decomposition products. The resulting PSCs showed stable characteristics beyond 1000 h in ambient air and over 3000 h at 60°C. Most notably, the introduction of spatial ALD at atmospheric pressure paves the way to the future roll-to-roll manufacturing of stable perovskite solar cells.

ASSOCIATED CONTENT

Saturation of ALD growth variating the amount of H_2O and TDMASn, Optical absorption and their respective Tauc plots for 20 nm SnO_x films, EQE data of PSCs comprising S-ALD based SnO_x, solar cell characteristics vs. time under elevated temperature, statistics of PSC, solar cell characteristics of PSCs vs. ALD deposition temperature, RBS/NRA data of impurities in S-ALD based SnO_x at different deposition temperatures.

AUTHOR INFORMATION

Corresponding Authors

*E-Mail: lhoffmann@uni-wuppertal.de (L.H)

*E-Mail: brinkmann@uni-wuppertal.de (K.O.B)

*E-Mail: t.riedl@uni-wuppertal.de (T.R.)

ACKNOWLEDGMENT

We acknowledge the German Federal Ministry for Education and Research (Grants No. 03EK3529E, 13N13819, and 13N12889) and the Deutsche Forschungsgemeinschaft (DFG) (Grants: RI1551/4-2) for financial support. P.G. acknowledges funding from the European Research Council (ERC) under the European Union's Horizon 2020 research and innovation programme (grant agreement No. 637367).

REFERENCES

(1) Shin, S. S.; Yeom, E. J.; Yang, W. S.; Hur, S.; Kim, M. G.; Im, J.; Seo, J.; Noh, J. H.; Seok, S. Il. *Science* **2017**, *356* (6334), 167–171.

(2) National Renewable Energy Laboratory. NREL Efficiency Chart.

(3) Stolterfoht, M.; Wolff, C. M.; Amir, Y.; Paulke, A.; Perdigón-Toro, L.; Caprioglio, P.; Neher, D. *Energy Environ. Sci.* **2017**, *10* (6), 1530–1539.

(4) Yang, W. S.; Park, B.-W.; Jung, E. H.; Jeon, N. J.; Kim, Y. C.; Lee, D. U.; Shin, S. S.; Seo, J.; Kim, E. K.; Noh, J. H.; Seok, S. Il. *Science* **2017**, *356* (6345), 1376–1379.

(5) Conings, B.; Drijkoningen, J.; Gauquelin, N.; Babayigit, A.; D'Haen, J.; D'Olieslaeger, L.; Ethirajan, A.; Verbeeck, J.; Manca, J.; Mosconi, E.; Angelis, F. De; Boyen, H.-G. *Adv.*

Energy Mater. **2015**, *5* (15), 1500477.

(6) Xu, J.; Buin, A.; Ip, A. H.; Li, W.; Voznyy, O.; Comin, R.; Yuan, M.; Jeon, S.; Ning, Z.; McDowell, J. J.; Kanjanaboos, P.; Sun, J.-P.; Lan, X.; Quan, L. N.; Kim, D. H.; Hill, I. G.; Maksymovych, P.; Sargent, E. H. *Nat. Commun.* **2015**, *6* (May), 7081.

(7) Niu, G.; Li, W.; Meng, F.; Wang, L.; Dong, H.; Qiu, Y. *J. Mater. Chem. A* **2014**, *2* (3), 705.

(8) Juarez-Perez, E. J.; Hawash, Z.; Raga, S. R.; Ono, L. K.; Qi, Y. *Energy Environ. Sci.* **2016**, *9* (11), 3406–3410.

(9) Xu, F.; Zhang, T.; Li, G.; Zhao, Y. *J. Mater. Chem. A* **2017**, *5* (23), 11450–11461.

(10) Niu, G.; Guo, X.; Wang, L. *J. Mater. Chem. A* **2015**, *3* (17), 8970–8980.

(11) Kato, Y.; Ono, L. K.; Lee, M. V.; Wang, S.; Raga, S. R.; Qi, Y. *Adv. Mater. Interfaces* **2015**, *2* (13), 1500195.

(12) Kim, A.; Lee, H.; Kwon, H.-C.; Jung, H. S.; Park, N.-G.; Jeong, S.; Moon, J. *Nanoscale* **2016**, *8* (12), 6308–6316.

(13) Aitola, K.; Domanski, K.; Correa-Baena, J.-P.; Sveinbjörnsson, K.; Saliba, M.; Abate, A.; Grätzel, M.; Kauppinen, E.; Johansson, E. M. J.; Tress, W.; Hagfeldt, A.; Boschloo, G. *Adv. Mater.* **2017**, *29* (17), 1606398.

(14) Bai, Y.; Dong, Q.; Shao, Y.; Deng, Y.; Wang, Q.; Shen, L.; Wang, D.; Wei, W.; Huang, J. *Nat. Commun.* **2016**, *7*, 12806.

(15) Domanski, K.; Correa-Baena, J.-P.; Mine, N.; Nazeeruddin, M. K.; Abate, A.; Saliba, M.; Tress, W.; Hagfeldt, A.; Grätzel, M. *ACS Nano* **2016**, *10* (6), 6306–6314.

(16) Grancini, G.; Roldán-Carmona, C.; Zimmermann, I.; Mosconi, E.; Lee, X.; Martineau, D.; Narbey, S.; Oswald, F.; De Angelis, F.; Graetzel, M.; Nazeeruddin, M. K. *Nat. Commun.* **2017**, *8*, 15684.

(17) Sanehira, E. M.; Tremolet de Villers, B. J.; Schulz, P.; Reese, M. O.; Ferrere, S.; Zhu, K.; Lin, L. Y.; Berry, J. J.; Luther, J. M. *ACS Energy Lett.* **2016**, *1* (1), 38–45.

(18) Bush, K. A.; Bailie, C. D.; Chen, Y.; Bowring, A. R.; Wang, W.; Ma, W.; Leijtens, T.; Moghadam, F.; McGehee, M. D. *Adv. Mater.* **2016**, *28* (20), 3937–3943.

(19) You, J.; Meng, L.; Song, T.-B.; Guo, T.-F.; Yang, Y. (Michael); Chang, W.-H.; Hong, Z.; Chen, H.; Zhou, H.; Chen, Q.; Liu, Y.; De Marco, N.; Yang, Y. *Nature Nanotechnology*. 2015, pp 75–81.

(20) Chen, W.; Wu, Y.; Yue, Y.; Liu, J.; Zhang, W.; Yang, X.; Chen, H.; Bi, E.; Ashraful, I.; Gratzel, M.; Han, L. *Science* **2015**, *350* (6263), 944–948.

(21) Bush, K. A.; Palmstrom, A. F.; Yu, Z. J.; Boccard, M.; Cheacharoen, R.; Mailoa, J. P.; McMeekin, D. P.; Hoye, R. L. Z.; Bailie, C. D.; Leijtens, T.; Peters, I. M.; Minichetti, M. C.; Rolston, N.; Prasanna, R.; Sofia, S.; Harwood, D.; Ma, W.; Moghadam, F.; Snaith, H. J.; Buonassisi, T.; Holman, Z. C.; Bent, S. F.; McGehee, M. D. *Nat. Energy* **2017**, *2* (4), 1–7.

(22) Knez, M.; Nielsch, K.; Niinistö, L. *Adv. Mater.* **2007**, *19* (21), 3425–3438.

(23) Meyer, J.; Görrn, P.; Bertram, F.; Hamwi, S.; Winkler, T.; Johannes, H.-H.; Weimann, T.; Hinze, P.; Riedl, T.; Kowalsky, W. *Adv. Mater.* **2009**, *21* (18), 1845–1849.

(24) Meyer, J.; Schmidt, H.; Kowalsky, W.; Riedl, T.; Kahn, a. *Appl. Phys. Lett.* **2010**, *96* (24), 243308.

(25) Kim, I. S.; Martinson, A. B. F. *J. Mater. Chem. A* **2015**, *3* (40), 20092–20096.

(26) Koushik, D.; Verhees, W. J. H.; Kuang, Y.; Veenstra, S.; Zhang, D.; Verheijen, M. A.; Creatore, M.; Schropp, R. E. I. *Energy Environ. Sci.* **2017**, *10* (1), 91–100.

(27) Chang, C. Y.; Lee, K. T.; Huang, W. K.; Siao, H. Y.; Chang, Y. C. *Chem. Mater.* **2015**, *27*

(14), 5122–5130.

(28) Kim, I. S.; Cao, D. H.; Buchholz, D. B.; Emery, J. D.; Farha, O. K.; Hupp, J. T.; Kanatzidis, M. G.; Martinson, A. B. F. *Nano Lett.* **2016**, *16* (12), 7786–7790.

(29) Behrendt, A.; Friedenberger, C.; Gahlmann, T.; Trost, S.; Becker, T.; Zilberberg, K.; Polywka, A.; Görrn, P.; Riedl, T. *Adv. Mater.* **2015**, *27* (39), 5961–5967.

(30) Brinkmann, K. O.; Zhao, J.; Pourdavoud, N.; Becker, T.; Hu, T.; Olthof, S.; Meerholz, K.; Hoffmann, L.; Gahlmann, T.; Heiderhoff, R.; Oszajca, M. F.; Luechinger, N. A.; Rogalla, D.; Chen, Y.; Cheng, B.; Riedl, T. *Nat. Commun.* **2017**, *8*, 13938.

(31) Hu, T.; Becker, T.; Pourdavoud, N.; Zhao, J.; Brinkmann, K. O.; Heiderhoff, R.; Gahlmann, T.; Huang, Z.; Olthof, S.; Meerholz, K.; Többens, D.; Cheng, B.; Chen, Y.; Riedl, T. *Adv. Mater.* **2017**, *29* (27), 1606656.

(32) Zhao, J.; Brinkmann, K. O.; Hu, T.; Pourdavoud, N.; Becker, T.; Gahlmann, T.; Heiderhoff, R.; Polywka, A.; Görrn, P.; Chen, Y.; Cheng, B.; Riedl, T. *Adv. Energy Mater.* **2017**, *7* (14), 1602599.

(33) Levy, D. H.; Freeman, D.; Nelson, S. F.; Cowdery-Corvan, P. J.; Irving, L. M. *Appl. Phys. Lett.* **2008**, *92* (19), 2006–2009.

(34) Hoffmann, L.; Theirich, D.; Pack, S.; Kocak, F.; Schlamm, D.; Hasselmann, T.; Fahl, H.; Räupke, A.; Gargouri, H.; Riedl, T. *ACS Appl. Mater. Interfaces* **2017**, *9* (4), 4171–4176.

(35) Wei, W.; Hu, Y. H. *Int. J. Energy Res.* **2017**, *41* (7), 1063–1069.

(36) Yang, J.; Siempelkamp, B. D.; Liu, D.; Kelly, T. L. *ACS Nano* **2015**, *9* (2), 1955–1963.

(37) Hoffmann, L.; Theirich, D.; Hasselmann, T.; Räupke, A.; Schlamm, D.; Riedl, T. *J. Vac. Sci. Technol. A* **2016**, *34* (1), 01A114.

(38) Jur, J. S.; Parsons, G. N. *ACS Appl. Mater. Interfaces* **2011**, *3* (2), 299–308.

(39) Hoffmann, L.; Theirich, D.; Schlamm, D.; Hasselmann, T.; Pack, S.; Brinkmann, K. O.; Rogalla, D.; Peters, S.; Räupke, A.; Gargouri, H.; Riedl, T. *J. Vac. Sci. Technol. A* **2018**, *36* (1), 01A112.

(40) Choi, D.; Maeng, W. J.; Park, J.-S. *Appl. Surf. Sci.* **2014**, *313*, 585–590.

(41) Poodt, P.; van Lieshout, J.; Illiberi, A.; Knaapen, R.; Roozeboom, F.; van Asten, A. *J. Vac. Sci. Technol. A* **2013**, *31*, 01A108.

(42) Elam, J. W.; Baker, D. a.; Hryn, A. J.; Martinson, A. B. F.; Pellin, M. J.; Hupp, J. T. *J. Vac. Sci. Technol. A* **2008**, *26* (2), 244.

TABLE OF CONTENTS